HHS Public Access

Author manuscript

Langmuir. Author manuscript; available in PMC 2015 September 30.

Published in final edited form as:

Langmuir. 2015 May 19; 31(19): 5440–5448. doi:10.1021/acs.langmuir.5b00095.

Analysis of Exosome Release as a Cellular Response to MAPK Pathway Inhibition

K. Agarwal, **M. Saji**, **S. M. Lazaroff**, **A. F. Palmer**, **M. D. Ringel**, and **M. E. Paulaitis***

William G. Lowrie Department of Chemical and Biomolecular Engineering, Department of Chemistry, Nanoscale Science and Engineering Center for Affordable Nanoenginering of Polymeric Biomedical Devices, Department of Internal Medicine, Division of Endocrinology Diabetes and Metabolism, Arthur G. James Comprehensive Cancer Center and Richard G. Solove Research Institute, The Ohio State University, Columbus, Ohio 43210, United States

Abstract

Exosome size distributions and numbers of exosomes released per cell are measured by asymmetric flow-field flow fractionation/multi-angle light scattering (A4F/MALS) for three thyroid cancer cell lines as a function of a treatment that inhibits MAPK signaling pathways in the cells. We show that these cell lines release exosomes with well-defined morphological features and size distributions that reflect a common biological process for their formation and release into the extracellular environment. We find that those cell lines with constitutive activation of the MAPK signaling pathway display MEK-dependent exosome release characterized by increased numbers of exosomes released per cell. Analysis of the measured exosome size distributions based on a generalized extreme value distribution model for exosome formation in intracellular multivesicular bodies highlights the importance of this experimental observable for delineating different mechanisms of vesicle formation and predicting how changes in exosome release can be modified by pathway inhibitors in a cell context-dependent manner.

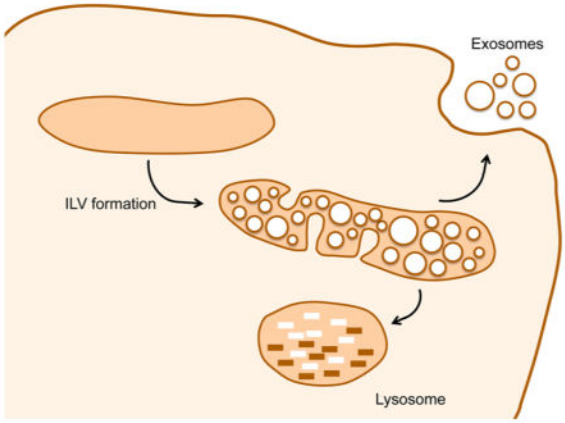

*Corresponding Author: paulaitis.1@osu.edu.

Present Address: (K.A.) KBI Biopharma, Durham, North Carolina 27704, United States.

The authors declare no competing financial interest.

I. INTRODUCTION

Recent discoveries of small RNAs in extracellular vesicles[1–4] have generated widespread interest in extracellular vesicles (EVs) as vehicles for intercellular communication. EV-mediated transfer of miRNA, in particular, has been implicated in cancer as a mechanism for promoting tumor metastasis and/or modulating immune responses, in addition to epigenetic reprograming cells in the tumor microenvironment.[5–8] EVs present in body fluids, such as blood or urine, have diagnostic potential as biomarkers in assays that are less invasive than tissue biopsies[9,10] and have therapeutic potential as natural delivery vehicles for proteins and nucleic acids,[11,12] making them potential candidates for cancer therapies.[13]

EVs consist primarily of exosomes and shedding vesicles that are released from all cell types in response to specific stimuli, but by entirely different mechanisms. Exosomes are secreted by the exocytosis of multivesicular bodies (MVBs), while shedding vesicles are formed by budding small cytoplasmic protrusions that then detach from the cell surface.[14,15] The biophysical properties of exosomes and shedding vesicles—notably, vesicle size and shape—reflect their distinct biogenesis pathways. Exosomes are generally defined by their spherical, unilamellar morphology, their size (average diameters less than ~100 nm), and the expression of specific biomarkers, including tetraspanins, whereas shedding vesicles are more heterogeneous in size and shape with characteristic lengths up to 1 μm.[14–17] Although the numbers of exosomes and larger vesicles released by individual cells will vary in a cell type- and cell state-dependent manner, current studies of EV-mediated miRNA transfer have not quantified these contributions or the anticipated heterogeneous distribution of miRNAs across and within the two subpopulations as a function of different stimuli.[18] Quantification of vesicle number concentrations as a function of vesicle size is an essential goal for clinical applications of exosomes as cancer biomarkers, which requires identifying the tumor-derived exosomes specifically and determining their numbers in patient samples.[19]

Biophysical characterizations of EVs typically include visualizing vesicle morphologies by electron microscopy, measuring vesicle size distributions, and, more recently, estimating absolute number concentrations. The first experimental observations of cell-secreted EVs by transmission electron microscopy (TEM) at ambient temperature describe them as spherical vesicles with a distinctive cup-shaped morphology that is an artifact of the sample preparation.[1,3,10,20] More recent studies at cryogenic temperatures (cryo-TEM), which preserve vesicle morphologies during preparation, have confirmed their unilamellar structure and spherical shape with EV diameters between ~20 and 150 nm and an electron-dense interior.[21–23]

Dynamic light scattering (DLS) is frequently used to measure EV size distributions in large part to confirm sampling the subpopulation of smaller EVs corresponding to exosomes.[20,24,25] EV hydrodynamic diameters obtained by DLS are based on translational diffusion coefficients derived from measured time correlation functions of light scattered by vesicles undergoing Brownian motion. The analysis of DLS measurements is straightforward for monodisperse populations of vesicles with a relatively narrow range of vesicle diameters, although the overall range of diameters that can be measured is extensive: 1 nm to 6 μm.[25] The interpretation of DLS measurements becomes more problematic,

however, for highly disperse vesicle populations, as well as for bimodal size distributions, because the intensity of light scattered from a solid (hollow) spherical vesicle depends on the sixth (fourth) power of its diameter. Thus, light scattered from a small number of larger vesicles can overwhelm light scattered from the smaller vesicles, resulting in an underestimate of the subpopulation of smaller vesicles in polydisperse samples.[25] Moreover, EV size distributions obtained by DLS are relative distributions; absolute vesicle number concentrations as a function of vesicle size are not determined.

Nanoparticle tracking analysis (NTA) is a more recent extension of DLS that has been applied to measure vesicle diameters from 50 nm to 1 μm.[4,24,26–28] Absolute vesicle number concentrations can also be obtained, and the latest instruments are capable of tracking antigen-specific EVs using fluorescently labeled antibodies if sufficient numbers of antigens are present,[24,26] in principle enabling EV surface markers to be correlated with vesicle size. NTA using light scattering for particle tracking will likewise be biased to larger vesicles, and measurements of vesicle concentrations are sensitive to the refractive index of the vesicles,[25] which may differ substantially across a heterogeneous population of EVs from different cell sources.[28]

In this article, we report the application of asymmetric flow-field flow fractionation coupled with multi-angle light scattering (A4F/MALS) to measure vesicle size distributions and vesicle number concentrations of the exosome subpopulation of EVs released by three thyroid cancer cell lines in response to a specific external stimulus. In asymmetric flow-field flow fractionation, laminar flow of a carrier fluid transports the EVs in a sample along a narrow channel, while hydrodynamic fractionation by vesicle size occurs by applying a cross-flow perpendicular to the direction of the channel flow.[29] As the cross-flow is gradually reduced, smaller vesicles in the sample move into faster flowstreams toward the center of the channel due to their greater Brownian motion, and consequently elute from the channel earlier than larger vesicles. The retention time in the channel, τ_r, and the vesicle diameter, d, are linearly related by Stokes' law and the channel and cross-flow volumetric flowrates, V_c and V_x, respectively:

$$\tau_r = \frac{\pi \eta w^2}{2 k_B T} \frac{V_x}{V_c} d, \quad (1)$$

where η is the viscosity of the carrier fluid, w the channel width, and $k_B T$ thermal energy (Boltzmann's constant times temperature). By first fractionating the sample based on vesicle size, A4F/MALS circumvents the vesicle size dependence of scattered light in DLS and NTA.[30–35] Quantitative measurements of vesicle number concentrations are attainable with an appropriate model for the single-vesicle scattering function that contains an accurate refractive index profile for the vesicle.

The BCPAP, TPC1, and FTC133 cell lines chosen for this study have different mutations derived from the common forms of thyroid cancer. These cell lines were selected based on their mutation status to quantify the number of exosomes released per cell in response to inhibiting the mitogen-activated protein kinase (MAPK) signaling pathway that plays a critical role in thyroid cancer initiation and progression. BCPAP cells express the BRAF

V600E mutation, which causes selective constitutive activation of MAPK signaling, while TPC1 cells express RET/PTC1, a gene rearrangement that causes constitutive activation of the Ret tyrosine kinase, which activates MAPK and PI3K signaling.[36,37] In contrast, FTC133 cells are driven by the selective activation of PI3K signaling through the mutation and loss of tumor suppressor PTEN.[36,37] Thus, whereas cancer cells, in general, are known to release exosomes at elevated levels compared to normal cells,[4,38] we expect to observe enhanced BCPAP and TPC1 cellular responses to inhibiting MAPK signaling manifested in the exosomes released by these cells relative to the untreated cells and the FTC133 cells if the MAPK signaling pathway plays a role in the release of exosomes from these cancer cells.

II. MATERIALS AND METHODS

II.1. Cell Culture

All cells were grown in culture media containing EV-depleted fetal bovine serum (FBS). Human thyroid carcinoma BCPAP, TPC1, and FTC133 cell lines were provided by Dr. R. Schweppe (University of Colorado, Denver) with permission from the following originating researchers: FTC133, P. Goretzki, University of Leipzig, Germany; BCPAP, D. N. Fabien, Centre Hospitalier Lyon-Sud, France; and TPC1, H. Sato, Kanazawa University, Japan. The three cell lines were independently confirmed for correct identification by DNA fingerprinting after receipt. BCPAP cells were grown in RPMI 1640 media supplemented with 1× MEM non-essential amino acids (NEAA, Life Technologies, Carlsbad, CA) in addition to 5% MV-depleted FBS, whereas the TPC1 and FTC133 cells were grown in DMEM media (Life Technologies, Carlsbad, CA) supplemented with NEAA and 5% MV-depleted FBS.[39] The cells at ~70% confluency were grown in 10 cm cell culture dishes for 24 h before isolating the EVs.

The U0126 MEK-specific inhibitor treatment (Cell Signaling Technology, Beverly, MA) was carried out as described in detail elsewhere.[40] Briefly, the cells in media containing EV-depleted FBS were treated with 20 μM U0126 for 24 h prior to EV isolation. An equivalent concentration of DMSO was added as a control treatment. Specific inhibition of MEK by U0126 was confirmed by Western blot of protein lysates isolated 24 h after treatment (data not shown). Cell viability and total cell numbers were determined using a Countess Automated Cell Counter (Life Technologies, Carlsbad, CA) and trypan blue exclusion assay under the same conditions. Cell viability was found be to greater than 90%.

II.2. Isolation of Extracellular Vesicles

EVs were isolated by sequential centrifugation/ultracentrifugation at 4 °C as described in detail elsewhere.[41] Briefly, cells were separated from the culture media by centrifugation at 300*g* for 5 min and 2000*g* for 20 min. The cell-free supernatant was then transferred to 25 mL polycarbonate ultracentrifuge tubes (Beckman Coulter, Brea, CA) and depleted of cell debris in a single spin at 10 000*g* for 30 min. The supernatant was then transferred to clean polycarbonate tubes and spun at 100 000*g* for 70 min to pellet the EVs. The supernatant from this spin was removed by aspiration, and the pellet was washed with sterile 1× PBS, resuspended, and then spun a second time at 100 000*g* for 70 min. The washed pellet was

resuspended in 1× PBS for cryo-TEM imaging and the A4F/MALS measurements. Each EV sample consisted of vesicles isolated from 50×10^6 to 150×10^6 cells (an average of 35 cell culture dishes) whereas the total number of cells for each sample was estimated by randomly selecting four dishes and counting cells per dish.

II.3. Asymmetric Flow-Field Flow Fractionation/Multi-Angle Light Scattering

EVs were fractionated based on vesicle size in a tapered separation channel 15.2 cm in length and widths at the inlet and outlet ports of 2.15 and 0.3 cm, respectively. The channel height was set by a 350 μm spacer above a regenerated cellulose membrane (10 kDa cutoff). All flowrates in the fractionation were controlled by the Eclipse 2 separation system (Wyatt Technology Corporation, Santa Barbara, CA) connected to an Agilent HPLC system 1100 series (Agilent Technologies, Santa Clara, CA), which consists of a G1320A isocratic pump and a G1313A autosampler. This instrument is coupled to an 18-angle static light scattering detector (15 angles are accessible using the flow cell) with a gallium arsenide laser at a wavelength of λ_0 = 658 nm (Dawn HELEOS) and a differential refractive index (dRI) detector (Optilab rEX, Wyatt Technology Corporation). The system was controlled by Eclipse software, version 2.6. Data was acquired and processed using Astra 5.3.4.20 software (Wyatt Technology Corporation).

EV fractionation was carried out by first conditioning the regenerated cellulose membrane with two sacrificial injections of bovine serum albumin (10 μg/μL), followed by 100 μL of the sample at a flow rate of 1.00 mL/min for 5 min and then focusing for 7 min, during which the carrier buffer (0.1 M PBS, pH 7.4 filtered through a 0.1 μm filter) enters through both the inlet and outlet ports of the channel to focus the sample near the injection point. Fractionation was accomplished at a constant channel flow rate of 1.00 mL/min by reducing the cross-flow rate from an initial value of 0.26 mL/min to 0.06 mL/min over an elution time of 45 min.

The fractionation efficiency was determined using monodisperse polystyrene standard beads 57, 102, and 200 nm in diameter (Thermo Fisher Scientific, Fremont, CA) diluted to particle numbers on the order of 10^9 to 10^{10} in 10 μL of 1× PBS containing 500 ppm sodium dodecyl sulfate (Life Technologies, Grand Island, NY). An efficiency of 49% was determined by comparing the known concentrations to particle counts obtained by MALS using the solid sphere model with a refractive index of 1.590 for the polystyrene beads.[31]

Mild sonication of the EV suspensions was carried out prior to the A4F/MALS measurements. Measurements on samples that were not sonicated beforehand resulted in size distributions that were systematically skewed toward higher fractions of larger EVs compared to sonicated samples, indicating the presence of loose aggregates that are dispersed with mild sonication.

EVs at low concentrations in the original sample are diluted further in asymmetric flow-field flow fractionation. Based on an average density of 1.13–1.19 g/mL for cell-secreted exosomes,[17] we estimate that the mass concentration of EVs in a typical A4F fraction is at most on the order of 10^{-6} g/mL. Thus, each fraction eluting from the A4F separation channel can be treated as a dilute solution of independent, non-interacting vesicles that have

a monodisperse size distribution. The intensity of light scattered from this dilute solution at an angle θ is defined in terms of the excess Rayleigh ratio,

$$R(\theta)=K*McP(\theta), \quad (2)$$

where K^* is an optical constant, M is the molar mass, c is the mass concentration, and $P(\theta)$ is the single-vesicle scattering function. The excess Rayleigh ratio is proportional to the intensity of light scattered at angle θ in excess of light scattered at the same angle by the solution in the absence of the vesicles.[42,43] The average diameter and number concentration of EVs in each fraction were derived from eq 2 using the coated-sphere model for $P(\theta)$ and refractive indexes of 1.354 for the EV interior[44] and 1.400 for the lipid bilayer.[28] A bilayer thickness of 5.5 (±0.69) nm was determined independently by direct measurements of the bilayer in cryo-TEM images of more than 50 EVs. A refractive index of 1.329 for the PBS buffer was measured directly using the dRI detector.

The vesicle number concentration was found to be most sensitive to the refractive index for the EV interior and to a lesser extent the refractive index of the lipid bilayer in the coated-sphere model. We estimate that an uncertainty of ±0.025 in the refractive index of the EV interior corresponds to an uncertainty of about one order of magnitude in the vesicle number concentration, whereas the same uncertainty in the refractive index of the lipid bilayer corresponds to an uncertainly of approximately ±20% in the vesicle number concentration. Relative concentrations of EVs derived from treated cells compared to untreated cells are, however, unaffected by the uncertainties in either refractive index.

The average vesicle diameter was found to be less sensitive to the two refractive indexes in the coated-sphere model, although more sensitive to the refractive index for the EV interior. An uncertainty of ±0.025 in the refractive index of the EV interior corresponds to an uncertainty of approximately ±10% in the average vesicle diameter, whereas the same uncertainty in the refractive index of the lipid bilayer corresponds to an uncertainly of approximately ±3% in the average vesicle diameter. The average diameter of EVs derived from treated cells compared to untreated cells is likewise unaffected by the uncertainties in either refractive index, as expected.

II.4. Cryo-Transmission Electron Microscopy

Vitrified cryo-TEM specimens were prepared by applying 4 μL of the EV suspensions to glow-discharged lacey carbon-coated copper grids (400 mesh, Pacific Grid-Tech, San Francisco, CA) and then flash-freezing in liquid ethane at controlled conditions (22 °C and 95% relative humidity) in an FEI Vitrobot Mark IV automated vitrification device (FEI, Hillsboro OR). The vitrified samples were stored under liquid nitrogen before transferring to a Gatan cryoholder (model 626.DH) and visualized in an FEI Tecnai G2 F20 ST TEM (FEI, Hillsboro OR). The microscope was operated at 200 kV and in low-dose mode to minimize radiation damage to the samples. Images were captured using a 4k × 4k Gatan Ultrascan CCD camera at magnifications of 38 000× and 43 000×.

EV size distributions were derived from the cryo-TEM images by directly measuring the diameter of each EV using ImageJ software. Direct visual inspection of each image enabled

identifying ice crystal formation, electron beam damage, particulate contaminants, disrupted or distorted vesicles, and other potential artifacts due to sample preparation, and those samples discarded. The diameter of an individual EV was defined as the distance between the outer edges of the bilayer on opposite sides of the vesicle. An uncertainty in the measured diameters was determined from multiple measurements over a range of EVs with different diameters and at four different orientations across each vesicle to obtain a standard deviation of ±1.2 nm over the entire range of EV diameters studied. All cryo-TEM images were obtained at the Liquid Crystal Institute, Kent State University, Kent, OH.

III. RESULTS AND DISCUSSION

A representative A4F/MALS elution profile—intensity of scattered light at 90° as a function of elution time—and the corresponding average diameter of the vesicles in each A4F fraction as a function of elution time are shown in Figure 1. Sample elution begins at 19 min, preceded by a small void peak in the elution profile that reflects the crossover from focusing mode to elution mode in the fractionation. A single prominent peak in the elution profile is observed at 26 min, followed by an asymptotic return to baseline as the cross-flow approaches zero at 53 min. As expected for fractionation based on vesicle size (eq 1), the average vesicle diameter in the eluting fractions increases linearly with elution time up to ~36 min,[29,33] and then remains essentially constant over the remainder of the elution time. The average vesicle diameter at the plateau ranges from 180–225 nm depending on the cell source, but is essentially independent of the inhibitor treatment.

Small, secondary peaks in the elution profiles for EVs from the TPC1 cells were also observed at 53 min as the profiles asymptotically return to baseline (Figure 4) indicating that a portion of the vesicle population consisting of larger vesicles (>200 nm in diameter) had not yet eluted from the channel. Incomplete elution of larger vesicles in the population of BCPAP cell-derived EVs was also observed with the elution profiles remaining slightly above baseline at 53 min. Factors that can lead to the incomplete elution of specific EV samples include vesicle aggregation and/or adsorption on the A4F channel membrane. Improved fractionation of the larger vesicles could be achieved to some extent by adjusting the A4F cross-flow and focus-flow rates. However, these flow rates were found to adversely affect the fractionation of smaller EVs in our samples. A consequence of optimizing the fractionations for the smaller EVs in our samples therefore is to limit quantitative determinations of vesicle diameters and number concentrations to EVs smaller than ~200 nm in diameter, which encompasses the exosome subpopulation of EVs of interest.

Debye plots of the excess Rayleigh ratio as a function of $\sin^2(\theta/2)$ are shown in Figure 2 for three fractions of EVs obtained at A4F elution times corresponding to the leading edge (22 min), the peak (26 min), and the trailing edge (38 min) of the elution profile in Figure 1. The Debye plot for the smaller EVs that elute at 22 min is essentially linear, with deviations from linearity noted for the smallest scattering angles. The Debye plots become progressively more non-linear for the fractions of larger EVs that elute at 26 and 38 min with the deviations at 26 min for the smallest scattering angles similar to those noted for the leading edge EV fraction at 22 min. The intercept and slope of these plots in the limit of $\sin^2(\theta/2) \rightarrow 0$ are proportional to the concentration and average diameter squared, respectively, of the

EVs in each fraction.[42] The significantly higher intercept for the EV fraction at the peak of the A4F elution profile and the prominent upward curvature as $\sin^2(\theta/2) \rightarrow 0$ for the EV fraction in the trailing edge of the A4F elution profile are therefore expected.

The coated-sphere model fits of the data, which are also shown in Figure 2, accurately describe the Debye plots for the leading edge and the peak EV fractions, but underpredict the upward curvature at small scattering angles in the Debye plot for the trailing edge fraction. The underprediction of the Debye plots as $\sin^2(\theta/2) \rightarrow 0$ for the late eluting, larger EVs using the coated-sphere model reinforces the limitation associated with optimizing the fractionations for the smaller EVs—i.e., quantitative determinations of vesicle diameters and number concentrations are constrained to EVs smaller than ~200 nm in diameter. Although the maximum standard error in the light scattering measurements for each angle, shown in the inset of Figure 2, increases significantly as $\sin^2(\theta/2) \rightarrow 0$, the magnitude of the standard error is relatively small and does not account for the differences between the model predictions and the data as $\sin^2(\theta/2) \rightarrow 0$. Moreover, the fits for all three EV fractions are essentially independent of whether all 15 scattering angles are used or the three smallest scattering angles are excluded. Similar results were obtained across all our EV samples, including EVs derived from both treated and untreated cells, and in an independent analysis of the data using the Rayleigh–Gans–Debye approximation[43,45] with the thin-shell model, which is not offered in the Astra software. We conclude that excluding the three smallest scattering angles in the coated-sphere model fits of our data for the subpopulation of EVs with diameters less than ~200 nm has only a minimal impact on the predicted vesicle diameters and number concentrations. For example, vesicle number concentrations in the peak A4F fraction predicted by the coated-sphere model excluding the three smallest scattering angles are found to change by less than 10% across all EV samples compared to the coated-sphere model predictions that include these angles.

Figure 3 compares vesicle size distributions derived from the A4F/MALS measurements to those obtained from cryo-TEM images for the exosome subpopulations of EVs from untreated TPC1 and BCPAP cells. Similar asymmetric, unimodal distributions are observed in both cases, although the peak in the A4F/MALS distributions is shifted slightly to larger exosome diameters relative to the corresponding peak in the cryo-TEM distributions. In addition, exosomes with diameters less than 45 nm that were frequently observed in the cryo-TEM images were not detected or were detected at much lower fractions by A4F/MALS. The lower resolution for these smaller exosomes in the A4F/MALS measurements coincides with the lower limit of detection in the light scattering measurements, which is ~1/20 of the wavelength of incident light,[30] or approximately 33 nm for our measurements. A small number of exosomes ranging from 185–205 nm in diameter are also detected in the A4F/MALS distribution for BCPAP EVs that are not found in the cryo-TEM distribution. Since only a small fraction of the sample is analyzed in the cryo-TEM images compared to A4F/MALS, the discrepancy may simply reflect the statistical limitation of the much smaller cryo-TEM sample size, although experimental bias introduced in the cryo-TEM sample preparation cannot be ruled out.[46,47] We conclude nonetheless that the exosome size distributions derived from the A4F/MALS measurements and from cryo-TEM images are in good agreement, with the A4F/MALS measurements biased to detecting slightly larger

vesicles and cyro-TEM images biased to slightly smaller vesicles. Notably, no vesicles smaller than 20 nm in diameter were observed in the cryo-TEM images.

Representative cryo-TEM images of the TPC1 and BCPAP cell-derived exosomes are also shown in Figure 3. The unilamellar structure and spherical shape characteristic of nearly all vesicles imaged stand out in contrast to the round, cup-shaped morphologies typically seen in TEM images.[1,3,10] The distinctive dark ring corresponding to the bilayer structure of the membrane is also clearly visible in these images and is a general observation. Another morphological feature observed in the vast majority of EV images is the appearance of darker regions of electron-dense material within the exosomes. The granularity of this encapsulated material suggests that these darker regions are not artifacts of imaging vesicles constrained by the thickness of the vitrified film, which can give the appearance of dark shadows in the vesicle interior.[48] No significant changes in these characteristic morphological features were observed in the cryo-TEM images of EVs derived from cells subjected to the inhibitor treatment.

Representative A4F/MALS elution profiles for exosomes released from untreated and U0126-treated TPC1 cells are shown in Figure 4. The two elution profiles are essentially identical, with a small secondary peak observed in both profiles at ~53 min, which indicates that a portion of the sample corresponding to a small number of larger vesicles does not elute from the A4F channel within the specified elution time. The effect of MAPK inhibition on the size distributions of exosomes released from TPC1 and BCPAP cells is shown in Figure 5. The total number of exosomes released per cell is given in Table 1 for both the untreated and U0126-treated cells. The tabulated results show that TPC1 and BCPAP cells release greater numbers of exosomes per cell in response to MAPK inhibition. These increases are not accompanied, however, by significant changes in the exosome size distributions, as shown in Figure 5. The total number of exosomes released per cell from TPC1 cells over 24 h increases two-fold relative to the number of untreated cells, whereas the corresponding increase for BCPAP cells is roughly three-fold. For FTC133 cells, no increase in the total number of exosomes released per cell over 24 h is observed when these cells are treated with the U0126 inhibitor.

The absolute numbers of exosomes released per cell from the untreated cells over 24 h (Table 1) are also comparable to those reported for other cancer cell lines under similar culture conditions where NTA was used to measure the numbers of vesicles released per cell over 48 h.[4] Assuming a constant rate of release over 48 h, medulloblastoma cells were found to release 6700–12 650 vesicles per cell and glioblastoma and melanoma cells released 3500–6500 vesicles per cell, whereaas normal human fibroblasts released 1900–3100 vesicles per cell over 24 h. Unimdodal vesicle size distributions over roughly similar ranges of vesicles diameters were also reported.

The measured exosome size distributions were analyzed by fitting them to the general form of extreme value distributions (EVDs).[49] EVDs emerge from models that assume vesicle size distributions depend on the method of vesicle preparation, and as such, have been used to describe size distributions of lipid vesicle formulations prepared by sonication, extrusion, and detergent dialysis.[33,50,51] Different physical models and mechanisms of vesicle

formation lead to different EVD expressions, which are defined by the sign of the shape parameter, ζ.[50–52] For the Frechet EVD, $\zeta > 0$, whereas for the Weibull EVD, $\zeta < 0$; and $\zeta = 0$ defines the Gumbel EVD.[49] The application of the general form of EVDs pursued here enables an unbiased determination of the EVD expression that best represents the measured exosome size distributions, and as such provides a framework for discriminating between physical models and mechanisms that can lead to these distributions.

A representative EVD fit of the measured size distribution of exosomes from untreated TPC1 cells is shown in Figure 6. The Frechet EVD ($\zeta > 0$) captures the distinct peak and the asymmetry in the distribution that characterizes the actual distribution. Also shown is a fit of the measured exosome size distribution using the Schulz distribution.[53,54] The Schulz distribution assumes the vesicles achieve an equilibrium size distribution that is likewise skewed to larger vesicles,[54] and thus serves as a benchmark for distinguishing equilibrium from non-equilibrium vesicle size distributions. In comparison to the Fréchet EVD, the Schulz distribution fit produces a broader distribution and fails to capture the abrupt cutoff in the actual distribution at a minimum vesicle diameter. The superior fit obtained with the Fréchet EVD represents a general finding in fitting the A4F/MALS data across all cell lines and for both the untreated and U0126-treated cells. In addition, the Fréchet EVD was identified as the only EVD to accurately reproduce the exosome size distributions measured in this study. Fréchet EVD parameters obtained from these fits are given in Table 2.

The Fréchet EVD description of the exosome size distributions suggests a mechanism for exosome formation that is distinctly different from the mechanism proposed for vesicles formed by sonication, extrusion, or detergent dialysis, which produce vesicle size distributions that are described by the Weibull EVD.[33,50,51] The Weibull description is based on a random fractionation model in which an upper limit to the vesicle diameter is defined. For vesicles prepared by sonication, $1.55 < -1/\zeta < 2.31$, depending on the lipid composition,[50,51] whereas for lipid vesicles prepared by extrusion, $1.10 < -1/\zeta < 1.62$, depending on the pore diameter of the membrane, or by dialysis, $1.03 < -1/\zeta < 2.94$, depending on the detergent.[33] The spherical vesicles that are formed in these preparations nonetheless span a range of diameters comparable to those obtained here for cell-derived exosomes.

We recently proposed a model for exosome formation based on microdomain-induced budding of the limiting membrane of intracellular multivesicular bodies (MVBs) that produces the Fréchet EVD description of exosome size distributions. [55] In this model, exosomes form as small microdomains coalesce into larger microdomains on the MVB limiting membrane, leading to the inward budding of the membrane to form internal or intraluminal vesicles.[56] These vesicles then detach from the limiting membrane to become exosomes internalized within the MVB. The Fréchet EVD description of exosome size distributions follows from the assumption that a growing microdomain must bud once it has reached a certain critical size, irrespective of the details of the coalescence mechanism(s),[57] and the identification of a minimum vesicle diameter related to this critical microdomain size. This minimum vesicle diameter, which likely reflects lipid packing constraints, is in contrast to the upper limit placed on the vesicle diameter in the fragmentation model for the Weibull EVD description. Our finding that the Fréchet distribution as opposed to the

Weibull distribution emerges from the generalized EVD fits of the measured exosome size distributions also implies that factors, such as the breakup of larger shedding vesicles or vesicles that may form during the centrifugation/ultracentrifugation steps in the EV isolation process, do not contribute significantly to the exosome subpopulation of EVs released by the untreated or U0126-treated thyroid cancer cells.

IV. CONCLUSIONS

We observe that untreated BCPAP, TPC1, and FTC133 thyroid cancer cells release vesicles with common, well-defined morphological features and size distributions that can be attributed to the exosome subpopulation of cell-derived EVs. Moreover, these morphological features and vesicle size distributions are not affected by the upregulated release of exosomes as a cellular response to inhibiting the constitutively activated MAPK signaling pathway in the BCPAP and TPC1 cells. The vast majority of exosomes derived from these cells are spherical in shape with a single bilayer membrane encapsulating electron-dense material. Further, the exosome size distributions obtained from A4F/MALS, as well as those generated from cryo-TEM images are without exception unimodal with exosomes <150 nm in diameter, an extended tail skewed to larger exosomes, and average exosome diameters between 61 and 76 nm. The experimental observable that characterizes the cellular responses to MAPK inhibition in the cells with constitutive MAPK activation (i.e., BCPAP and TPC1 cells) is the release of increased numbers of exosomes/cell. The absence of this response in the FTC133 cells, which do not have constitutive activation of MAPK, suggests a cell-autonomous exosome release response to MAPK inhibitors that may be predicted by pathway activation. This result is consistent with the concept of “oncogene addiction” of cancer cell lines.[58,59]

Our analysis of the measured exosome size distributions using the general form of EVDs identified the Fréchet distribution and a model for exosome formation based on the inward budding of the limiting membrane of intracellular MVBs to form vesicles, which then detach to become exosomes internalized within the MVB. That the Fréchet distribution emerges from this unbiased fitting of the size distributions rather than the Weibull EVD and a model for exosome formation based on random fragmentation of larger vesicles supports the conclusion that fragmentation of larger vesicles, such as shedding vesicles, that could occur during the centrifugation/ultracentrifugation steps in the EV isolation process does not contribute significantly to the exosome subpopulation of EVs released from these thyroid cancer cells. Measuring the lipid and protein compositions of this subpopulation of EVs and comparing them to the lipid and protein compositions of the fraction of EVs that elutes from the A4F channel at later times will be a key experiment to confirm that no other sources contribute to the exosome subpopulation derived from both untreated cells and especially U0126-treated cells. The current analysis nonetheless highlights the utility of measuring and characterizing exosome size distributions as a means to test different mechanisms of exosome formation.

Finally, we have shown the potential of A4F/MALS as a biophysical characterization technique for enumerating EVs as a function of size over a range of vesicle diameters from 40 to 200 nm. Asymmetric flow-field flow fractionation by size of polydisperse EV samples

generates dilute, monodisperse subpopulations that can be straightforwardly analyzed to give vesicle number concentrations provided an accurate model for the single-vesicle form factor is available. Since the vesicle number concentration is sensitive to the refractive index or refractive index profile of the vesicle used in any model, a critical requirement for accurate determinations of vesicle number concentrations is accurate refractive index measurements for the specific EVs of interest. In this study, we used the coated-sphere model with reasonable estimates for the refractive index of the lipid bilayer and the inner core of the vesicle and with the bilayer thickness determined independently from cryo-TEM images by direct measurements of the bilayer. Exosome size distributions derived from A4F/MALS using this model were found to be in good agreement with distributions generated directly from cryo-TEM images of representative populations of exosomes. We also note that the performance of asymmetric flow-field flow fractionation can be sensitive to changes in EV properties. Thus, suitable A4F performance may require preliminary experiments to determine optimal operating parameters for different samples. For example, EV samples from the same three thyroid cancer cell lines treated with an inhibitor for another signaling pathway produced strikingly different A4F elution profiles. The ability to tune the A4F operating conditions to achieve the optimal fractionation of EV samples from a wide variety of cell sources and cell states is nonetheless an advantage of the technique.

Acknowledgments

This work was supported by grants from the NIH (P01 CA124570 and 1RC2AG036559-01 to M.D.R. and 1UH2TR000914-01) and the NSF (EEC-0425626 and EEC-0914790 to M.E.P.). We thank Dr. Min Gao at the Liquid Crystal Institute, Kent State University, for numerous helpful discussions and valuable training in cryo-TEM experiments.

References

1. Valadi H, Ekstrom K, Bossios A, Sjostrand M, Lee JJ, Lotvall JO. Exosome-mediated transfer of mRNAs and microRNAs is a novel mechanism of genetic exchange between cells. Nat Cell Biol. 2007; 9:654–659. [PubMed: 17486113]
2. Skog J, Wurdinger T, van Rijn S, Meijer D, Gainche M, Sena-Esteves L, Curry W, Carter B, Krichevsky A, Breakefield X. Glioblastoma microvesicles transport RNA and proteins that promote tumour growth and provide diagnostic biomarkers. Nat Cell Biol. 2008; 10:1470–1476. [PubMed: 19011622]
3. Gibbings DJ, Ciaudo C, Erhardt M, Voinnet O. Multivesicular bodies associate with components of miRNA effector complexes and modulate miRNA activity. Nat Cell Biol. 2009; 11:1143–1149. [PubMed: 19684575]
4. Balaj L, Lessard R, Dai L, Cho YJ, Pomeroy SL, Breakefield XO, Skog J. Tumour microvesicles contain retro-transposon elements and amplified oncogene sequences. Nat Commun. 2011; 2:1–9.
5. Kogure T, Lin WL, Yan IK, Braconi C, Patel T. Intercellular nanovesicle-mediated microRNA transfer: a mechanism of environmental modulation of hepatocellular cancer cell growth. Hepatology. 2011; 54:1237–1248. [PubMed: 21721029]
6. Yang M, Chen J, Su F, Yu B, Lin L, Liu Y, Huang JD, Song E. Microvesicles secreted by macrophages shuttle invasion-potentiating microRNAs into breast cancer cells. Mol Cancer. 2011; 10:1476–4598.
7. Grange C, Tapparo M, Collino F, Vitillo L, Damasco C, Deregibus MC, Tetta C, Bussolati B, Camussi G. Microvesicles released from human renal cancer stem cells stimulate angiogenesis and formation of lung premetastatic niche. Cancer Res. 2011; 71:5346–5356. [PubMed: 21670082]
8. Rana S, Malinowska K, Zoller M. Exosomal tumor microRNA modulates premetastatic organ cells. Neoplasia. 2013; 15:281–295. [PubMed: 23479506]

9. Mitchell PS, Parkin RK, Kroh EM, Fritz BR, Wyman SK, Pogosova-Agadjanyan EL, Peterson A, Noteboom J, O'Briant KC, Allen A, Lin DW, Urban N, Drescher CW, Knudsen BS, Stirewalt DL, Gentleman R, Vessella RL, Nelson PS, Martin DB, Tewari M. Circulating microRNAs as stable blood-based markers for cancer detection. Proc Natl Acad Sci US A. 2008; 105:10513–10518.
10. Taylor DD, Gercel-Taylor C. MicroRNA signatures of tumor-derived exosomes as diagnostic biomarkers of ovarian cancer. Gynecol Oncol. 2008; 110:13–21. [PubMed: 18589210]
11. Andre F, Chaput N, Schartz NE, Flament C, Aubert N, Bernard J, Lemonnier F, Raposo G, Escudier B, Hsu DH, Tursz T, Amigorena S, Angevin E, Zitvogel L. Exosomes as potent cell-free peptide-based vaccine. I. Dendritic cell-derived exosomes transfer functional MHC class I/peptide complexes to dendritic cells. J Immunol. 2004; 172:2126–2136. [PubMed: 14764678]
12. Pegtel DM, Cosmopoulos K, Thorley-Lawson DA, van Eijndhoven MA, Hopmans ES, Lindenberg JL, de Gruijl TD, Wurdinger T, Middeldorp JM. Functional delivery of viral miRNAs via exosomes. Proc Natl Acad Sci US A. 2010; 107:6328–6333.
13. Ristorcelli E, Beraud E, Verrando P, Villard C, Lafitte D, Sbarra V, Lombardo D, AV. Human tumor nanoparticles induce apoptosis of pancreatic cancer cells. FASEB J. 2008; 22:3358–3369. [PubMed: 18511551]
14. Cocucci E, Racchetti G, Meldolesi J. Shedding microvesicles: artefacts no more. Trends Cell Biol. 2010; 19:43–51. [PubMed: 19144520]
15. Raposo G, Stoorvogel W. Extracellular vesicles: exosomes, microvesicles, and friends. J Cell Biol. 2013; 200:373–383. [PubMed: 23420871]
16. Witwer KW, Buzás EI, Bemis LT, Bora A, Lässer C, Lötvall J, Nolte-'t Hoen EN, Piper MG, Sivaraman S, Skog J, Théry C, Wauben MH, Hockberg F. Standardization of sample collection, isolation and analysis methods in extracellular vesicle research. J Extracell Vesicles. 2013; 2:20360.
17. Bobrie A, Théry C. Exosomes and communication between tumours and the immune system: are all exosomes equal? Biochem Soc Trans. 2013; 41:263–267. [PubMed: 23356294]
18. Chevillet JR, Kang Q, Ruf IK, Briggs HA, Vojtech LN, Hughes SM, Cheng HH, Arroyo JD, Meredith EK, Gallichotte EN, Pogosova-Agadjanyan EL, Morrissey C, Stirewalt DK, Hladik F, Yu EY, Higano CS, Tewari M. Quantitative and stioichiometric analysis of the microRNA content of exosomes. Proc Natl Acad Sci US A. 2014; 111:14888–14893.
19. Sverdlov ED. Amedio Avogadro's cry: What is a μg of exosomes? BioEssays. 2012; 34:873–875. [PubMed: 22815202]
20. Atay S, Cicek GT, Mehmet K, Douglas DT. Morphologic and proteomic characterization of exosomes released by cultured extravillous trophoblast cells. Exp Cell Res. 2011; 317:1192–1202. [PubMed: 21276792]
21. Conde-Vancells J, Rodriguez-Suarez E, Embade N, Gil D, Matthiesen R, Valle M, Elortza F, Lu SC, Mato JM, Falcon-Perez JM. Characterization and comprehensive proteome profiling of exosomes secreted by hepatocytes. J Proteome Res. 2008; 7:5157–5166. [PubMed: 19367702]
22. Coleman BM, Hanssen E, Lawson VA, Hill AF. Prion-infected cells regulate the release of exosomes with distinct ultrastructural features. FASEB J. 2012; 26:4160–4173. [PubMed: 22767229]
23. Kadiu I, Narayanasamy P, Dash PK, Zhang W, Gendelman HE. Biochemical and Biologic Characterization of Exosomes and Microvesicles as Facilitators of HIV-1 Infection in Macrophages. J Immunol. 2012; 189:744–754. [PubMed: 22711894]
24. Gercel-Taylor C, Atay S, Tullis RH, Kesimer M, Taylor DD. Nanoparticle analysis of circulating cell-derived vesicles in ovarian cancer patients. Anal Biochem. 2012; 428:44–53. [PubMed: 22691960]
25. van der Pol E, Coumans F, Varga Z, Krumrey M, Nieuwland R. Innovation in detection of microparticles and exosomes. J Thromb Haemost. 2013; 11:36–45. [PubMed: 23809109]
26. Dragovic RA, Gardiner C, Brooks AS, Tannetta DS, Ferguson DJ, Hole P, Carr B, Redman CW, Harris AL, Dobson PJ, Harrison P, Sargent IL. Sizing and phenotyping of cellular vesicles using nanoparticle tracking analysis. Nanomedicine. 2011; 7:780–788. [PubMed: 21601655]

27. Soo CY, Song Y, Zheng Y, Campbell EC, Riches AC, Gunn-Moore F, Powis SJ. Nanoparticle tracking analysis monitors microvesicle and exosome secretion from immune cells. Immunology. 2012; 136:192–197. [PubMed: 22348503]
28. Gardiner C, Ferreira YJ, Dragovic RA, Redman CW, Sargent IL. Extracellular vesicle sizing and enumeration by nanoparticle tracking analysis. J Extracell Vesicles. 2013; 2:1–11.
29. Giddings J, Yang F, Myers M. Flow-field-flow fractionation: a versatile new separation method. Science. 1976; 193:1244–1245. [PubMed: 959835]
30. Wyatt PJ. Light scattering and the absolute characterization of macromolecules. Anal Chim Acta. 1993; 272:1–40.
31. Shortt DW, Roessner D, Wyatt PJ. Absolute measurement of diameter distributions of particles using a multiangle light scattering photometer coupled with flow field-flow fractionation. Am Lab. 1996; 28:21–28.
32. Wyatt PJ. Submicrometer particle sizing by multiangle light scattering following fractionation. Colloid Interface Sci. 1998; 197:9–20.
33. Korgel BA, van Zanten JH, Monbouquette HG. Vesicle size distributions measured by flow field-flow fractionation coupled with multiangle light scattering. Biophys J. 1998; 74:3264–3272. [PubMed: 9635780]
34. Wyatt, PJ.; Weida, MJ. Method and Apparatus for Determining Absolute Number Densities of Particles in Suspension. US Patent. 6,774,994. Aug 10. 2004
35. McEvoy M, Razinkov V, Wei Z, Casas-Finet JR, Tous GI, Schenerman MA. Improved particle counting and size distribution determination of aggregated virus populations by asymmetric flow field-flow fractionation and multiangle light scattering techniques. Biotechnol Prog. 2011; 27:547–554. [PubMed: 21302365]
36. Saji M, Ringel MD. The PI3K-Akt-mTOR pathway in initiation and progression of thyroid tumors. Mol Cell Endocr. 2010; 321:20–28.
37. Schweppe RE, Klopper JP, Korch C, Pugazhenthi U, Benezra M, Knauf JA, Fagin JA, Marlow LA, Copland JA, Smallridge RC, Haugen BR. Deoxyribonucleic Acid Profiling Analysis of 40 Human Thyroid Cancer Cell Lines Reveals Cross-Contamination Resulting in Cell Line Redundancy and Misidentification. J Clin Endocr Metab. 2008; 93:4331–4341. [PubMed: 18713817]
38. Kharaziha P, Ceder S, Li Q, Panaretakis T. Tumor cell-derived exosomes: A message in a bottle. Biochim Biophys Acta, Rev Cancer. 2012; 1826:103–111.
39. McCarty SK, Saji M, Zhang X, Jarjoura D, Fusco A, Vasko VV, Ringel MD. Group I p21-activated kinases regulate thyroid cancer cell migration and are overexpressed and activated in thyroid cancer invasion. Endocr -Relat Cancer. 2010; 17:989–999. [PubMed: 20817787]
40. Braga-Basaria M, Hardy E, Gottfried R, Burman KD, Saji M, Ringel MD. 17-Allylamino-17-demethoxygeldanamycin activity against thyroid cancer cell lines correlates with heat shock protein 90 levels. Endocr Metab. 2004; 89:2982–2988.
41. Théry, C.; Amigorena, S.; Raposo, G.; Clayton, A. Current Protocols in Cell Biology. Vol. Chapter 3. John Wiley; Hoboken, NJ: 2006. Isolation and Characterization of Exosomes from Cell Culture Supernatants and Biological Fluids.
42. Podzimek, S. Light Scattering, Size Exclusion Chromatography and Asymmetric Flow Field Flow Fractionation. John Wiley & Sons; Hoboken, NJ: 2011.
43. Kerker, M. The Scattering of Light. Academic Press; New York: 1969.
44. Meglinski, I.; Doronin, A. Monte Carlo Modeling of Photon Migration for the Needs of Biomedical Optics and Biophotonics. In: Wang, KR.; Tuchin, VV., editors. Advanced Biophotonics: Tissue Optical Sectioning. Vol. 19. CRC Press; Boca Raton, FL: 2014. p. 1-58.Series in Optics and Optoelectronics
45. Berne, BJ.; Pecora, RR. Dynamic Light Scattering. Dover Publications; New York: 2000.
46. Mittal, V.; Matso, NB. Analytical Imaging Techniques for Soft Matter Characterization. Springer-Verlag; Berlin: 2012.
47. Kuntsche J, Horst JC, Bunjes H. Cryogenic transmission electron microscopy (cryo-TEM) for studying the morphology of colloidal drug delivery systems. Int J Pharm. 2011; 417:120–137. [PubMed: 21310225]

48. Almgren M, Edwards K, Karlsson G. Cryo-transmission electron microscopy of liposomes and related structures. Colloids Surf, A. 2000; 174:3–21.
49. Kotz, S.; Nadarajah, S. Extreme Value Distributions: Theory and Applications. Imperial College Press; London: 2000.
50. Tenchov BG, Yanev TK. Weibull Distribution of Particle Sizes Obtained by Uniform Random Fragmentation. J Colloid Interface Sci. 1986; 111:1–7.
51. Tenchov BG, Yanev TK, Tihova MG, Koynova RD. A probability concept about size distributions of sonicated lipid vesicles. Biochim Biophys Acta. 1985; 816:122–130. [PubMed: 4005231]
52. Sear RP. Generalization of Levine's prediction for the distribution of freezing temperatures of droplets: a general singlular model for ice nucleation. Atmos Chem Phys. 2013; 13:7215–72237.
53. van Zanten JH. The Zimm plot and its analogs as indicators of vesicle and micelle size polydispersity. J Chem Phys. 1998; 102:9121–9128.
54. Helfrich W. Size distributions of vesicles: the role of the effective rigidity of membranes. J Phys (Paris). 1986; 47:321–329.
55. Paulaitis ME, Agarwal K, Gao M, Saji M, Ringel MD. Nucleation model for exosome formation based on microdomain-induced budding of the MVB membrane. in preparation.
56. Huotari J, Helenius A. Endosome maturation. EMBO J. 2011; 30:3481–3500. [PubMed: 21878991]
57. Lipowsky R. Domain-induced budding of fluid membranes. Biophys J. 1993; 64:1133–1138. [PubMed: 19431884]
58. Weinstein IB, Joe A. Oncogene addiction. Cancer Res. 2008; 68:3077–3080. [PubMed: 18451130]
59. Vivanco I. Targeting molecular addictions in cancer. Br J Cancer. 2014; 111:2033–2038. [PubMed: 25268375]

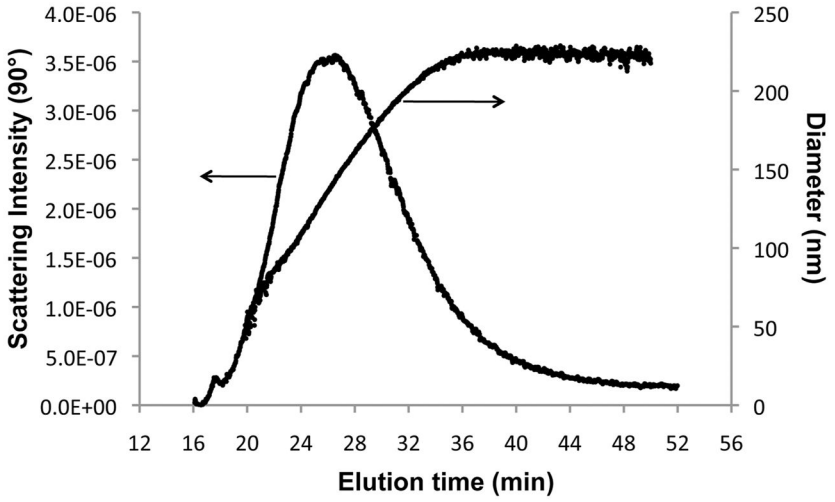

Figure 1.

Representative A4F/MALS elution profile of the scattered light intensity detected at a scattering angle of $\theta = 90°$ and the average vesicle diameter as a function of A4F elution time for EVs derived from untreated FTC133 cells. Average vesicle diameters are calculated using the coated-sphere model in the Astra 5.3.4.20 software.

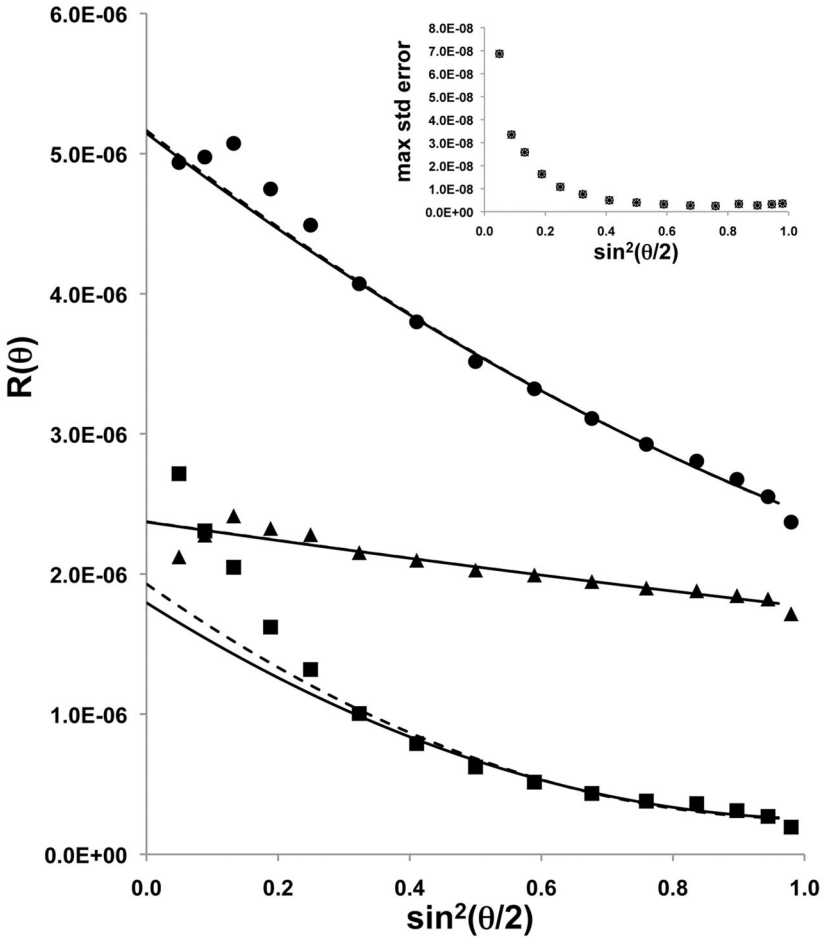

Figure 2.

Debye plots of the excess Rayleigh ratio $R(\theta)$ as a function of $\sin^2(\theta/2)$ for three A4F fractions obtained at elution times corresponding to the peak at 26 min (circles), the leading edge at 22 min (triangles), and the trailing edge at 38 min (squares) of the elution profile shown in Figure 1 for EVs derived from untreated FTC133 cells. The dashed lines represent fits of the data over all 15 scattering angles using the coated-sphere model in the Astra 5.3.4.20 software, and the solid lines represent fits of the data excluding the three smallest scattering angles. Inset: maximum standard error for each scattering angle as a function of $\sin^2(\theta/2)$. The symbols for the three fractions—peak (o), leading edge (×), and trailing edge (+)—overlap at each angle.

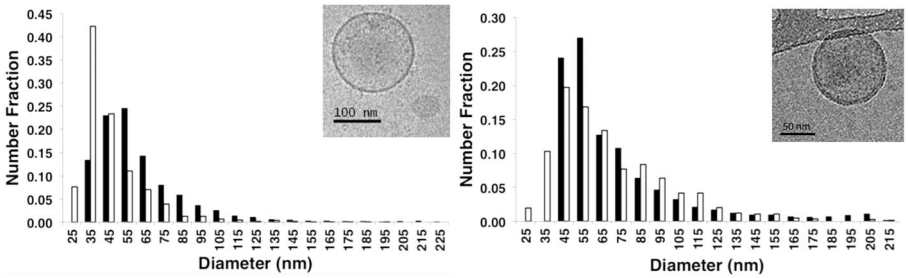

Figure 3.

Comparisons of the number fraction of vesicle diameters derived from the A4F/MALS measurements using the coated-sphere model (filled bars) to the number fraction of vesicle diameters obtained from cryo-TEM images (open bars) for the exosome subpopulation of EVs from untreated TPC1 (left) and BCPAP (right) cells (n = 1387 for the cryo-TEM images of TPC1 exosomes and n = 1079 for the cryo-TEM images of BCPAP exosomes). Representative cryo-TEM images depicting the unilamellar structure and spherical shape of the exosomes from each cell line are also shown.

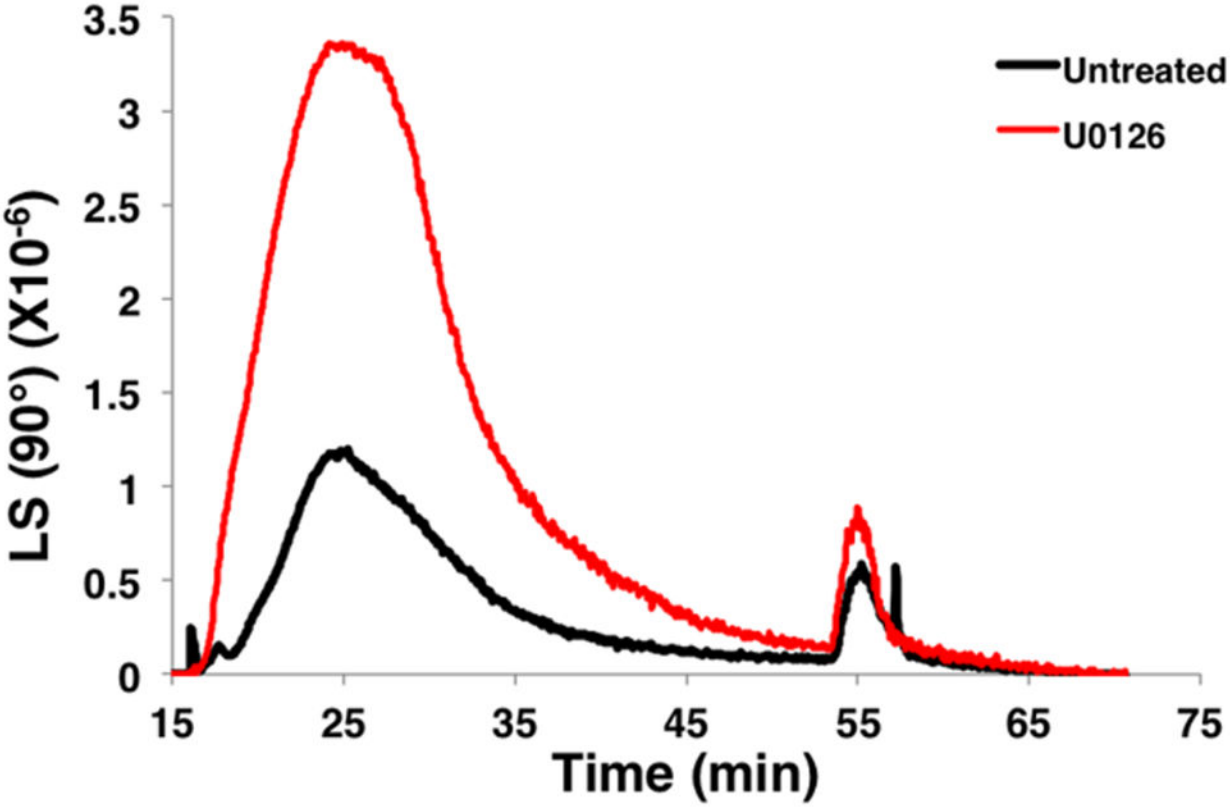

Figure 4.

Representative A4F/MALS elution profiles of the scattered light intensity detected at a scattering angle of $\theta = 90°$ as a function of the elution time for exosomes from untreated and U0126-treated TPC1 cells. The difference in the magnitude of $I(90°)$ reflects different concentrations of vesicles injected into the A4F channel, which range from 1.2×10^{10} to 3.4×10^{10} vesicles in the 100-μL sample volume for these experiments.

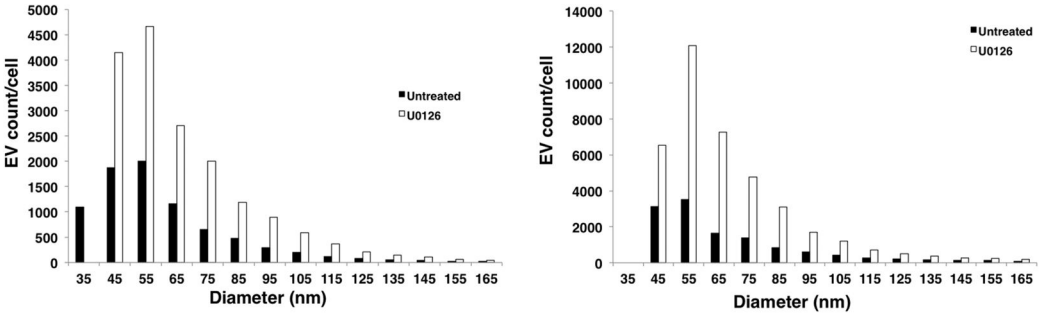

Figure 5.

Exosome size distributions for EVs from U0126-treated and untreated cells. Left: TPC1 cell-derived exosome size distributions (number of vesicles/cell) over 24 h in EV-depleted serum-containing medium. Right: BCPAP cell-derived exosome size distributions (number of vesicles/cell) over 24 h in EV-depleted serum-containing medium.

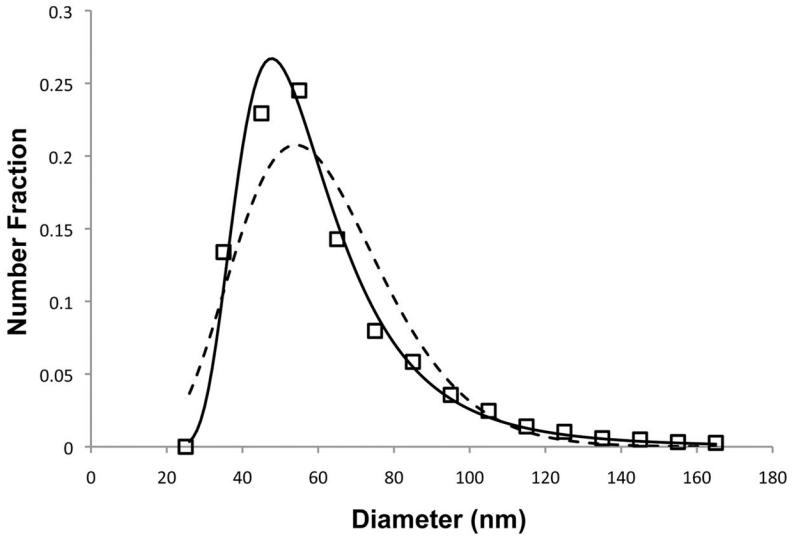

Figure 6.

Representative fit of the measured size distribution of exosomes from untreated TPC1 cells obtained by A4F/MALS using the general form of EVDs (solid line) compared to the Schulz distribution (dashed line). The Frechet EVD (solid line) with $\zeta = 0.180$, $\mu = 49.5$, and $\sigma = 14.0$ (Table 2) was found to give the best fit of the experimental data.

Table 1

A4F/MALS Measurements of Average Exosome Diameters and the Total Number of Exosomes Released per Cell over 24 h in Media Supplemented with EV-Depleted Serum.[a] Cells were treated with the U0126 MEK inhibitor (n = 2 except for vesicles derived from the treated FTC133 cells, where n = 1, and for vesicles derived from treated BCPAP cells where n = 3).

	average exosome diameter (nm)	total number of exosomes/cell
TPC1 Exosomes		
untreated cells	61 (±20)	7550–8500
U0126-treated cells	66 (±21)	15 000–18 500
BCPAP Exosomes		
untreated cells	67 (±22)	8700–15 900
U0126-treated cells	68 (±20)	29 500–49 000
FTC133 Exosomes		
untreated cells	76 (±24)	6200–7360
U0126-treated cells	72 (±23)	4200

[a]The exosome subpopulation of EVs is defined as vesicles ≤150 nm in diameter. The total number of exosomes per cell corresponds to the number collected over the entire A4F elution time from 19 to 53 min.

Table 2

Parameters of the General Form of the EVD Obtained from Fits of the Exosome Size Distributions Measured by A4F/MALS

	ζ	μ	σ	mean diameter[a] (nm)
TPC1 Exosomes				
untreated cells	0.180	49.5	14.0	61
U0126-treated cells	0.444	53.8	11.3	69
BCPAP Exosomes				
untreated cells	0.610	52.8	10.8	75
U0126-treated cells	0.287	56.3	12.1	68
FTC133 Exosomes				
untreated cells	0.054	65.0	19.5	77
U0126-treated cells	0.213	60.1	15.3	73

[a]The mean diameters are computed from the EVD probability distributions with these parameters.